RESEARCH ARTICLE

Surface deformation under overlapping impacts of solid particles

Xuerui ZANG[1], **Xuewen CAO**[1,*], **Zhenqiang XIE**[1], **Jun ZHANG**[2], **Farzin DARIHAKI**[2], **Yang LIU**[1]

[1] *College of Pipeline and Civil Engineering, China University of Petroleum (East China), Qingdao 266580, China*

[2] *Erosion/Corrosion Research Center, The University of Tulsa, Tulsa 74104, USA*

© The author(s) 2022.

Abstract: To improve the accuracy of erosion prediction, the effect of subsequent particles impacting the same area while the first single particle rebounds from the substrate must be considered. This issue has rarely been considered in studies pertaining to erosion damage. In the present study, the ABAQUS software is used to investigate the erosion crater morphology and stress distribution on a target material subjected to overlapping impacts of spherical particles. Subsequently, the validated model is applied to investigate the effect of the overlapping impacts of particles on the target. Accordingly, the correlation between erosion severity and the impact locations of the two incident particles is quantified. The results show that the horizontal distance between two solid particle impact locations can significantly affect the erosion magnitude and pattern. The interactions of the resulting craters diminish when the horizontal distance exceeds 0.6 times the particle diameter. When the horizontal distance is approximately 0.06 times the particle diameter, the energy loss originating from collisions reaches the maximum, which modifies the crater morphology. The present study is expected to provide in-depth insights into erosion mechanisms and erosion modeling.

Keywords: overlapping impact; spherical particle; surface morphology; energy dissipation; ABAQUS simulation

1 Introduction

Studies have shown that erosion is one of the most significant causes of material damage and equipment failure [1–3]. Erosion is a typical form of damage to oil and gas pipelines [4–6]. Solid particles transported by fluid impact the pipe wall, which may cause local damages such as small cracks, plastic deformation, and material shedding to the inner wall of the pipe. The continuous impact of particles will cause wall damage to accumulate gradually until the material fails, thereby resulting in significant economic losses and safety issues. Previous investigations indicated that erosion is a complex problem that is affected by particle velocity, angular velocity, impact angle, particle shape, and particle size. Theories based on experiments and simulations have been proposed to

model and predict material damage [7]. To accurately predict and manage erosive events in industrial processes, the erosion process must be investigated comprehensively, including the examination of the impact process and its relevant affecting factors, such as the particle diameter, impact kinetics, and energy conversion. The objectives are to determine the relationship between the aforementioned factors and the impact damage as well as to further generalize a user-friendly model to predict future events. In this regard, most of the currently available theoretical models focus on the particle shape, impact velocity, and impact angle [8–11], including the micro-cutting model [12], deformation wear theory [13, 14], plastic deformation accumulation theory [15–17], and adiabatic shear theory [18]; these models reveal the effect of abrasive particles on erosion and wear mechanisms.

---

* Corresponding author: Xuewen CAO, E-mail: caoxw@upc.edu.cn

清華大學出版社 Tsinghua University Press ⌒ Springer

Nomenclature

A, B, n	Train hardening at reference strain rate	K	Stiffness coefficient representing attribute of spring
A_0	Contact area between particle and material	K_B	Constant related to velocity of particle before collision
a	Radius of smallest cross-section of pattern	K_0	Empirical constant related to material properties
BH	Brinell hardness of material	m	Thermal softening of material
C	Strain rate of material	m_P	Quality of abrasive particle
D	Particle diameter	N_c	Effective number of turns, which is equal to the total number of turns minus two
D_m	Middle diameter, which is equal to the outer diameter minus the wire diameter		
D_1–D_5	Damage constants	n_1	Empirical constant related to material properties
d	Damage parameter	n_2	Empirical constant related to impact velocity
d_t	Damage parameters at time t	P	Pressure on surface of material
d_w	Wire diameter	Q_P	Formation of permanent indentation, which requires a certain amount of energy
d_0	Initial diameter		
d_1	Final diameter after deformation	R	Notch radius of smallest cross-section of pattern
E_C	Energy dissipated by time-dependent deformation (creep, swelling, and viscoelasticity) at $E_C = 0$	T_m	Melting temperature
		T_r	Reference temperature
		T^*	Normalized temperature
E_{FD}	Energy dissipated by friction	t	Duration of impact process
E_I	Remaining energy, which is known as the internal energy	u	Horizontal distance between the two impact events
E_K	Kinetic energy	v_P	Average impact velocity of particles
E_P	Energy dissipated by plasticity	v_0	Impact velocity
E_{QB}	Energy dissipated by damping effect of solid medium infinite elements	v'	Velocity of particle after impact
		W_D	Wear due to repeated deformation
E_S	Applied elastic strain energy	W_t	Initial kinetic energy of particles
E_{total}	Total energy	W_u	Increased internal energy of target material
E_U	Dissipated portion of internal energy	α	Impact angle of particles
E_V	Energy dissipated by viscous effects, $E_V = 0$	ε	Equivalent plastic strain rate
E_W	Work performed by external forces on body	ε_B	Deformation wear factor
ER	Ratio of mass loss of target material to mass of erosion particles	ε_{el}	Elastic stress
		ε_f	Fracture strain
F	Applied force	ε_{pl}	Equivalent plastic strain
F_s	Coefficient related to shape of particles	ε_0	Reference strain rate
$F(\alpha)$	Function of impact angle	η	Energy conversion rate
H_1	Penetration depth of first single particle	σ	Static yield stress
H_2	Penetration depth of second particle	σ_c	Total elastic stress
G	Rigidity modulus of wire	σ_u	Elastic stress
		σ^*	Stress triaxiality

Researchers have experimentally investigated different impact particles and target materials. Hutchings and Winter [19] investigated the impact of a single square particle on a low-carbon steel specimen.

Different impact parameters such as the impact angle and particle azimuth were investigated, and it was discovered that the impact process comprised two stages: forward spin impact and backspin impact.

Sahoo et al. [20] performed sandblasting experiments to statistically evaluate the behavior of particles impacting the target material, as well as investigated the effects of different parameters, including microstructural degradation, impact velocity, impingement angle, and erodent size on the material. Tirupataiah et al. [21] incorporated the effects of hardness, elastic modulus, and impact velocity into a theoretical model and established a functional correlation for the crater recovery degree. Papini and Dhar [22, 23] used a pneumatic launcher to investigate the erosion mechanism of angular particles based on an impact velocity of less than 100 m/s. Despite the achievements of the study, it was limited to the "rigid-plastic" framework.

Generally, experiments provide limited information, such as the impact velocity and crater depth, which cannot provide adequate information for analyzing dynamic erosion. Meanwhile, studies have indicated that the finite element method [24–29] can provide detailed information, including stress, interaction force, and crater morphology of particles and target materials [30–33]. In addition, it can be used to effectively investigate the effect of the abovementioned parameters on the target material. Many scholars [34–38] applied the finite element method to establish an erosion calculation model for angular particles that impact viscoplastic materials. The results obtained were verified via collision tests using an air gun. The effects of the impact angle and azimuth angle of the particles on the deformation mechanism of the target material were reflected in their numerical simulation and experiment. Previously, material removal [39, 40] and accumulation deformation [41–45] mechanisms caused by abrasive particles have been investigated

comprehensively. Most previous investigations focused on non-overlapping particle impacts on the target material, i.e., erosion modeling based on single-particle impact [46–48]. Figure 1(a) shows a schematic illustration of a completely non-overlapping impact with an extremely large horizontal distance, which hindered the crater interaction and its effect on the erosion profile from being considered.

The ultimate goal of this study is to quantify the neighboring impact of particles on erosion, which can be incorporated to the erosion model based on the single-particle impact. Therefore, we assumed that the particle impact velocity can be quantified accurately. Under this condition, the general form of a single-particle erosion model is typically expressed as Eq. (1):

$$ER = K_0 \left(BH \right)^{n_1} F_s v_p^{n_2} F\left(\alpha \right) \tag{1}$$

where ER is the ratio of the mass loss of the target material to the mass of the erosion particles; F_s is a coefficient related to the shape of the particles; BH is Brinell hardness of the material; K_0 and n_1 are the empirical constants related to the material properties; and v_p is the average impact velocity of the particles. Moreover, n_1 is an empirical constant related to the material properties; n_2 is an empirical constant related to the impact velocity; and $F(\alpha)$ is a function of the impact angle. As shown, the interaction between adjacent craters is rarely considered.

Therefore, in this study, a numerical model was established to investigate the overlapping impact of spherical particles, as shown in Fig. 1(b). The complex particle impact scenario was simplified to the impact of two neighboring particles. The expansion and
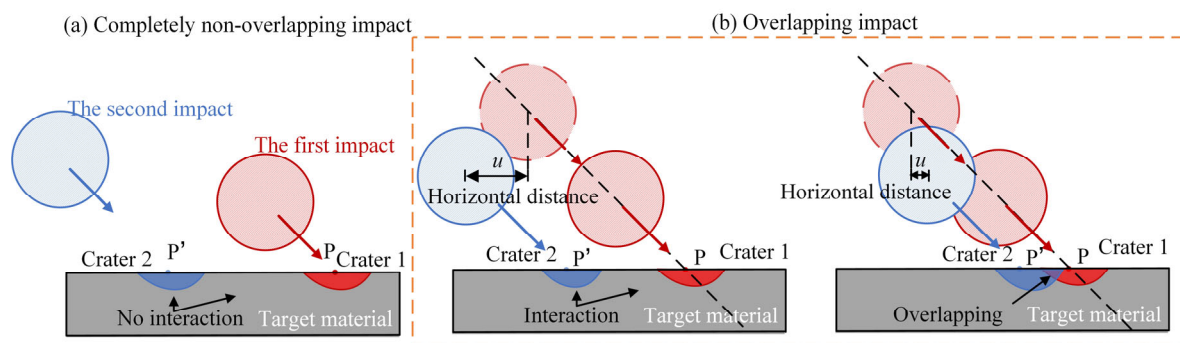

Fig. 1 Schematic illustrations of (a) completely non-overlapping impact and (b) overlapping impact.

addition of an impacting particle couplet were assumed. Therefore, it is critical to first investigate erosion damage by two overlapping impact particles comprehensively to understand the trend and results quantitatively. Different impact parameters, including the impact velocity, impact angle, and horizontal distance between two impacts, were considered to investigate the resulting erosion profile under multi-particle impacts. The present study is expected to provide a scientific basis for interpreting material erosion originating from multi-particle impacts as well as for elucidating the erosion mechanism.

2 Experimental background

2.1 Experimental device

The experimental setup used in this study was designed and manufactured based on the slingshot ejection device proposed by Dhar et al. [49]. Figure 2 shows the configuration of the test setup. During the experiment, the ejection rod was manually loaded by pressing the launching arm down until it was securely locked in place to the release mechanism (rubber arm stop). The ejection rod was connected to two springs in series and was limited by an adjustable plate. Moreover, the particles were fixed by a bracket (particle holder). The target fixing plate was fixed on the frame of the ejection rod, and the target frame (target holder) was adjustable to change the incident angle.

The ejector rod pressed the spring down to convert the elastic potential energy of the spring into the kinetic energy of the particles. It is noteworthy that different ejection speeds can be obtained by changing
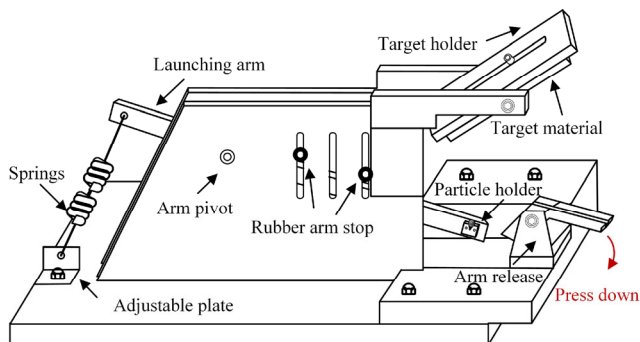
the spring elasticity. The spring constant is defined as Eq. (2):

$$K = \frac{G \times d_w^{\ 4}}{8 \times D_m^3 \times N_c} \tag{2}$$

where K is the stiffness coefficient representing the attribute of the spring, N/mm; G denotes the rigidity modulus of the wire, N/mm²; d_w is the wire diameter, mm; D_m is the middle diameter, which is equal to the outer diameter minus the wire diameter, mm; and N_c is the effective number of turns, which is equal to the total number of turns minus 2. The specific parameters of the spring are shown in Table 1.

2.2 Experimental process

In the experiments, particles were synthesized using high-speed steel (W18Cr4V), and a target material composed of 6061 aluminum alloy (AA6061) were used. The target material was selected to achieve the excellent plastic deformation performance. Therefore, the hardness of the target material should be lower than that of the particles. In this case, the particles can generate pits on the target material after the impact. Prior to the experiment, the target material was polished to obtain a smooth surface. The friction coefficient between the two materials was 0.1. The simulation results were consistent with the experimental results. Table 2 presents the main parameters of the particles and target materials.

Confocal microscopy (MicroPhase, PhaseView, France) was performed in the present study to scan the target material. Table 3 lists the experimental data. Meanwhile, Fig. 3 illustrates the morphology of the crater when the target was impacted by particles of 5 mm in diameter, where the impact angle and velocity were 45° and 20 m/s, respectively. The red

Fig. 2 Schematic illustration of ejection device.

Table 1 Parameters of spring.

Spring type	Wire diameter (mm)	Outside diameter (mm)	Length (mm)	Impact velocity (m/s)
1	2.1	18	80	14
2	2.5	25	85	16
3	3.2	25	87	18
4	3.2	25	90	20
5	3.2	25	95	22

Table 2 Mechanical properties of particles and target material.

Material	AA6061 (target material)	W18Cr4V (particles)
Morphology	—	Spherical
Density (kg/m^3)	2,700	7,850
Young's modulus (GPa)	70	206
Brinell hardness (N/mm^2)	30	650
Poisson's ratio	0.33	0.22

Table 3 Experimental settings.

Impact velocity (m/s)	Penetration depth (μm)	Standard deviation (μm)
14	36±2	4.8
16	39±2	4.4
18	45±2	4.8
20	61±2	5.2
22	73±2	5.0
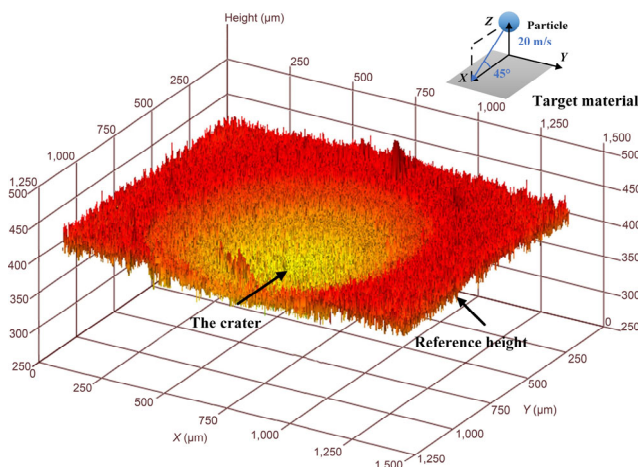
Fig. 3 Experimental results for the particle size of 5 mm, impact speed of 20 m/s, and impact angle of 45°.

and yellow areas indicate the non-impacted surface and the crater that is deeper than the non-impacted area, respectively.

3 Numerical simulation

Particle impact is a complex phenomenon. Accordingly, several theories have been proposed to model contact and damage mechanics [50, 51]. The Johnson-Cook (JC) viscoplastic model is used to model the flow stress behavior of typical metals subjected to large strains [52, 53]. To reduce the computational cost, a two-dimensional (2D) model was applied to the

calculations involved. In fact, the same calculations were performed by Takaffoli and Papini [54]. The modelling details are provided in the following sections.

3.1 Constitutive models

The strain of the target material changes significantly during dynamic erosion. To characterize materials at higher strain rates, the JC constitutive model, which is suitable for ductile metal materials [55–58], is used to characterize the nonlinear dynamic mechanical behavior of the materials. The present study focuses on ductile material erosion behavior. Therefore, the material constants for the JC constitutive model of AA6061 were obtained.

3.1.1 JC hardening criterion

Johnson and Cook [52] combined viscoplastic and continuum damage mechanics, and proposed an empirical constitutive model under a large deformation, a high strain rate, and thermal insulation [59, 60]. In this model, the yield flow stress of the material can be expressed as a function of the strain, strain rate, and temperature, as Eqs. (3) and (4):

$$\sigma = \left(A + B\varepsilon_{pl}^n \right)\left(1 + C\ln\frac{\varepsilon}{\varepsilon_0} \right)\left[1 - (T^*)^m \right] \tag{3}$$

$$T^* = \frac{T - T_r}{T_m - T_r} \tag{4}$$

where σ and ε_{pl} are the static yield stress and equivalent plastic strain, respectively. Moreover, A, B, and n denote the material parameters at the transition temperature; C and m are the strain rate and thermal softening of the material, respectively; ε is the equivalent plastic strain rate; ε_0 is the reference strain rate. Finally, T, T^*, T_m, and T_r denote the operating, normalized, melting, and reference temperatures, respectively.

The defined parameters were acquired via tensile and split Hopkinson bar tests on AA6061. The parameters of the JC hardening criterion are listed in Table 4.

Table 4 Parameters of JC hardening criterion.

Material	A	B	C	m	n	ε_0	T_m (K)	T^* (K)	T_r (K)
AA6061	335	85	0.012	1	0.11	1	925	300	292

3.1.2 JC damage criterion

The JC damage model is based on the cavitation growth and damage evolution principles of the material. In this model, the effects of stress triaxiality, strain rate, and temperature softening are considered. The failure criterion and calculation equations for the JC model are expressed as Eqs. (5)–(7):

$$\varepsilon_f = \left[D_1 + D_2 \exp\left(D_3 \sigma^*\right) \right] \left(1 + D_4 \ln \frac{\varepsilon}{\varepsilon_0}\right)\left(1 + D_5 T^*\right) \quad (5)$$

$$\sigma^* = \frac{1}{3} + \ln\left(1 + \frac{a}{2R}\right) \quad (6)$$

$$\varepsilon_f = 2\ln \frac{d_0}{d_1} \quad (7)$$

where ε_f and σ^* denote the fracture strain and stress triaxiality, respectively; D_1, D_2, D_3, D_4, and D_5 are the damage constants; a and R denote the radius and notch radius of the smallest cross-section of the pattern, respectively; d_0 and d_1 are the initial and final diameters after deformation, respectively. It is noteworthy that constants D_1–D_5 can be obtained using Eq. (5). Moreover, Eqs. (6) and (7) show the expressions for obtaining σ^* and ε_f, respectively. Table 5 lists the values of these parameters.

Table 5 Parameters of JC damage criterion [61].

Material	D_1	D_2	D_3	D_4	D_5	ε_0
AA6061	−0.77	1.45	0.47	0	1.6	1

3.2 Boundary conditions

In all the simulations, it was assumed that the particles were rigid bodies. In other words, the particle strain was set to zero during the impact. The initial velocity was applied to the particles through a predefined field, and the input velocity was decomposed along the X- and Y-directions. The movements of both the left and right sides were restricted along the X-direction, and the bottom plane was fixed. Figure 4 shows the imposed boundary conditions.

3.3 Mesh independence test and experimental verification

3.3.1 Mesh independence test

In numerical simulations, the use of a finer grid yields more accurate results, although at the expense of higher computational costs. In this study, a systematic grid independence test was performed to obtain a reasonable mesh size to ensure accuracy while maintaining a reasonable computational cost. In this regard, the von Mises stress and maximum depth were considered for selecting the optimized mesh. As shown in Table 6, five mesh sizes were considered in the grid-independence test. It is noteworthy that quadrilateral structural meshes were applied in all the simulations.

Figure 5(a) shows significant deviations in the von Mises stress contours between the results obtained from Test Nos. 1 and 2, indicating that the meshes were coarse.

Table 6 shows that for Test Nos. 1–3, the von Mises stress near the deformation ranged from 110 to 160 MPa after the second impact, whereas the von Mises stresses in Test Nos. 4 and 5 were 172.8 and 173.2 MPa, respectively, and their distributions were similar. As shown in Fig. 5(b), for Test Nos. 1–3, the depths of the target material ranged from 30 to 65 μm after the
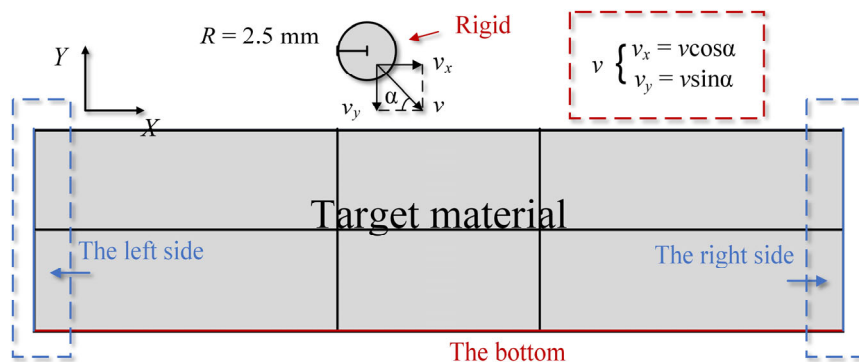

Fig. 4 Schematic illustration of 2D model with imposed boundary conditions.

Table 6 Parameters used in mesh convergence test.

Test No.	Contact region in *X*-axis direction	Contact region in *Y*-axis direction	Total number of elements	Computational cost (s)	Von Mises stress (MPa)
1	100	50	7,150	66	116.3
2	143	71	13,148	234	130.0
3	200	100	24,150	1,003	154.6
4	333	167	62,436	4,790	172.8
5	1,000	500	540,600	116,194	173.2
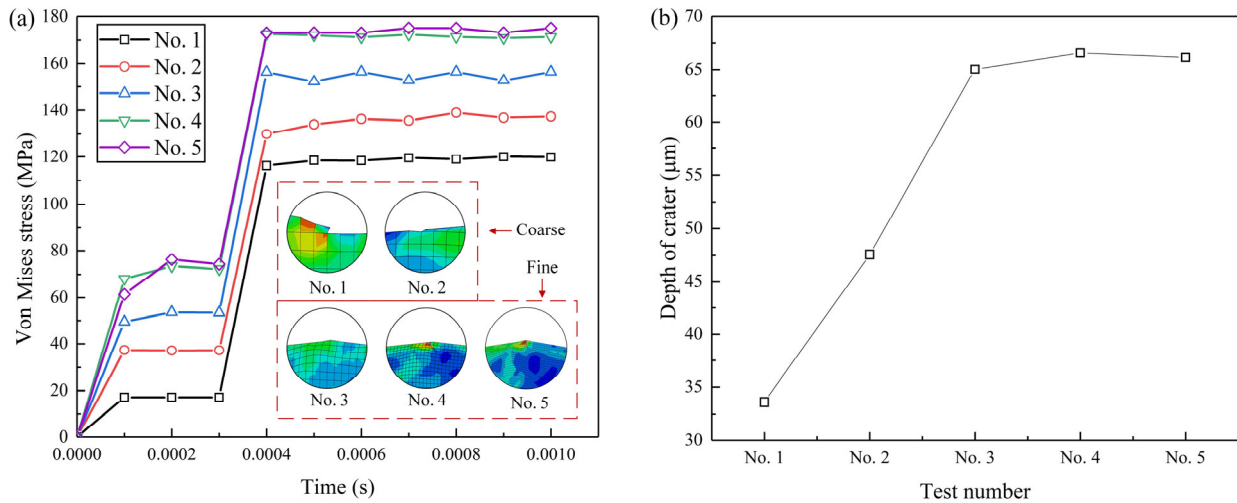
Fig. 5 Mesh convergence test curve based on the particle size of 5 mm, impact angle of 45°, and impact velocity of 20 m/s: (a) stress distribution for different mesh sizes; (b) the crater depth for different mesh sizes.

second impact. Meanwhile, for Test Nos. 4 and 5, the depths were 66.58 and 66.15 μm, respectively. When the number of elements was 62,436 (Test No. 4), the variations in both the von Mises stress and penetration is slight (within 2%) and hence negligible. This indicates that the calculation results were not sensitive to the number of meshes. However, the computational cost of Test No. 5 significantly surpassed that of the other mesh sizes. Hence, Test No. 4 was adopted in the models.

Figure 6 shows the mesh generated for the 2D target material. A quadrilateral structural mesh was applied in the simulations. It is noteworthy that CPS4R is a four-node bilinear plane stress quadrilateral element with reduced integration. Therefore, only one integral point exists in the center of the unit and hourglass control. Consequently, the element can resist deformation without involving the stiffness. In this type of unit, the analysis accuracy is affected less when the mesh is deformed, and the displacement can be solved accurately. To improve the calculation accuracy and conserve computational
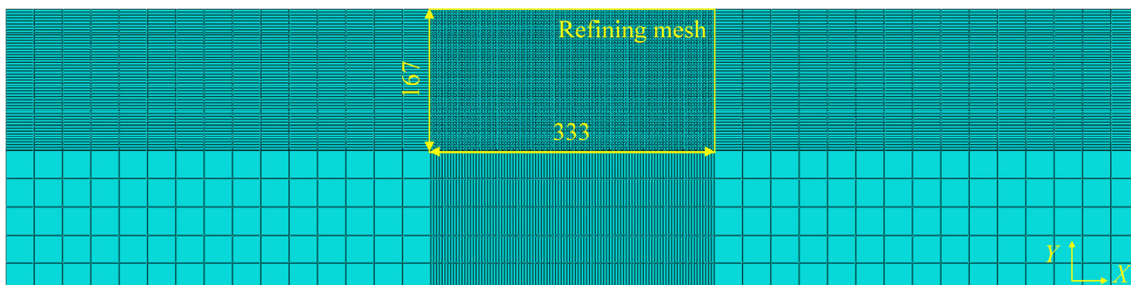
Fig. 6 Illustration of target material mesh.

resources, only finer meshes were applied in the contact area, whereas coarse meshes were applied in other areas. The total number of elements in the refined and fine meshes in the contact region were 62,436 and 55,611, respectively.

3.3.2 Experimental verification

In this study, numerical simulations were conducted under an impact angle of 45° and impact velocities of 14, 16, 18, 20, and 22 m/s. The results obtained were compared with the experimental results. Figure 7(a) shows the experimental impact results based on a velocity of 20 m/s. As shown, the crater depth and length created by a single particle impacting the target material were 61.0 and 1,352.5 μm, respectively. Meanwhile, Fig. 7(b) shows the simulation results under the same conditions, where a crater depth and length of 66.0 and 1,317.4 μm, respectively, are indicated. It was discovered that the depth and length

differences between the simulation and experiment results of the crater were 5.0 and 35.1 μm, respectively, which were only 8% and 3% greater compared with the experimental data. Therefore, the simulated value was consistent with the experimental value. It is noteworthy that the roughness data shown in Fig. 7 are expressed in units of micrometers, which are three orders of magnitude smaller compared with the units of the particle; therefore, they are negligible. Moreover, the effect of roughness is not considered in erosion models. Therefore, scholars typically characterize the effect of roughness using the friction coefficient [62, 63].

Figures 8 and 9 show the penetration depths and lengths under different incident velocities, respectively. The experiments were repeated five times for each group. The results show that the test values of the five groups (involving different speeds) agreed well with the numerical values obtained from the ABAQUS software. When the speed was 22 m/s, the maximum difference between the penetration depths was approximately 8 μm, indicating a 6% error compared with the experiment. Additionally, when the speed was 16 m/s, the maximum difference between the pitting lengths was approximately 49.0 μm, indicating a 4% error compared with the experiment.

A 2D model is a simplified model. However, as verified using data, it can capture the prediction of the maximum erosion depth and profile within the
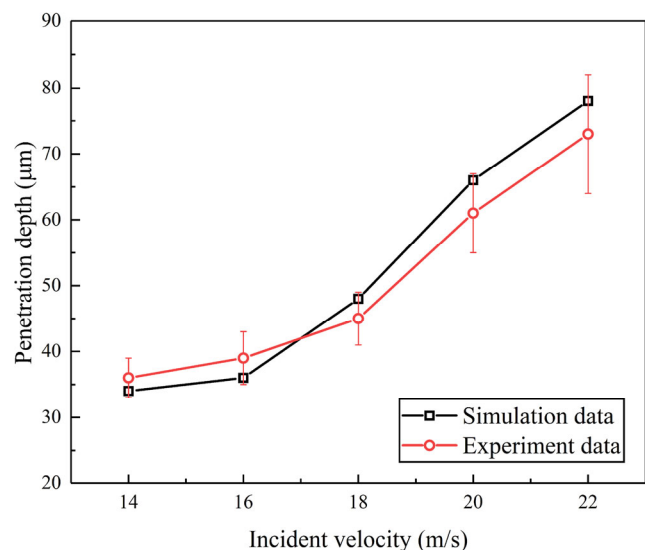

Fig. 7 Crater morphology obtained from single particle experiment and simulation: (a) experimental results and (b) simulation results of single-particle based on the particle size of 5 mm, impact velocity of 20 m/s, and impact angle of 45°.

Fig. 8 Distribution of penetration depth against incident velocity for the particle size of 5 mm, impact velocity of 14–22 m/s, and impact angle of 45°.
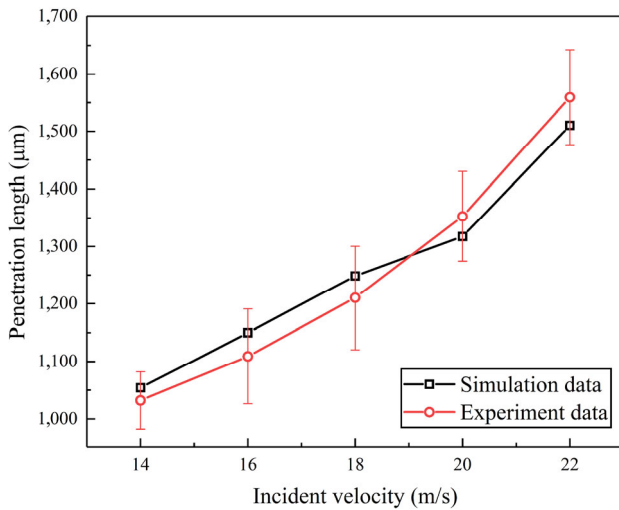
Fig. 9 Distribution of penetration length against incident velocity for the particle size of 5 mm, impact velocity of 14–22 m/s, and impact angle of 45°.
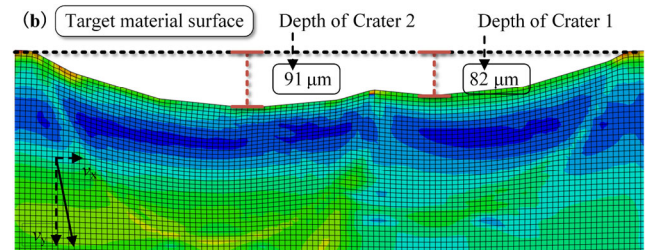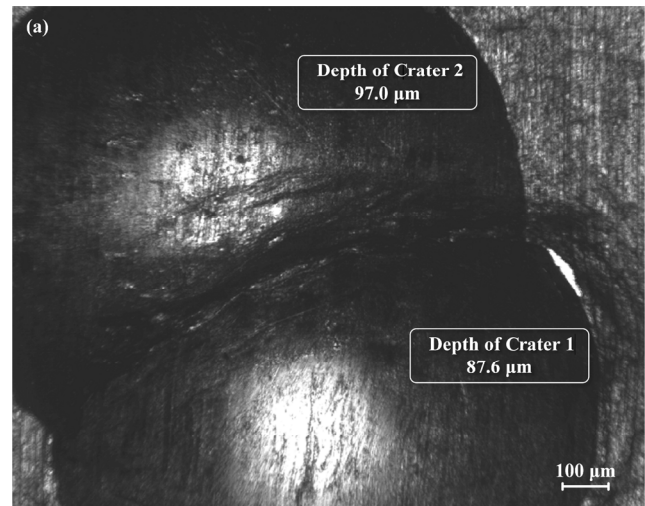

Fig. 10 Crater morphology obtained via experiment and simulation for overlapping impacts of spherical particles (Craters 1 and 2 are caused by the first and second impact events, respectively, for completely overlapping impacts caused by Craters 1 and 2 stacked together): (a) experimental results and (b) simulation results of overlapped particles with the particle size of 5 mm, horizontal impact distance of 1 mm, impact velocity of 20 m/s, and impact angle of 85°.
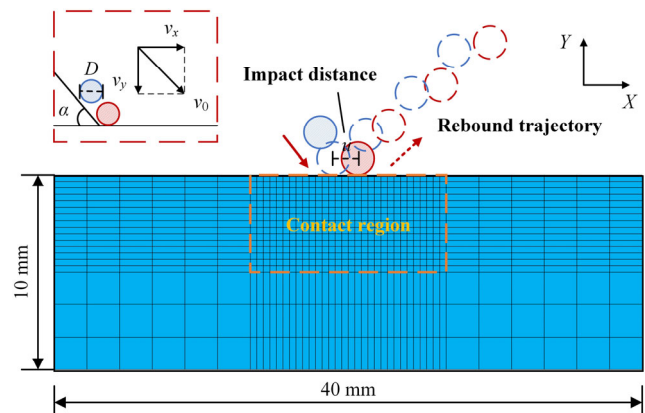
cross section. Owing to its relative accuracy, ability to represent the general trend, and reduced computational cost, it was used to present the results of the current study, similar to other previous studies [28, 40].

Figure 10 shows a comparison between the experimental results and simulation data for the overlapping impacts of spherical particles. In this experiment, the particle size and horizontal distance of the impact were 5 and 1 mm, respectively. Moreover, the impact velocity and angle were 20 m/s and 85°, respectively. After the two impact events, the depths of the crater yielded by the first and second impact events were 87.6 and 97.0 μm, respectively; moreover, the depths obtained from the simulation results were 82 and 91 μm, respectively. Therefore, the deviation between the two results remained within 6 μm. In summary, the 2D model can be used to effectively calculate material damage during impact processes.

3.4 Impact process

Figure 11 shows the impact process of the two particles. It was assumed that the material and size of the particles were the same in the two collisions. The red and blue balls represent the particles of the first and second impact events, respectively, with different positions of impact on the target material. D and u denote the particle diameter and horizontal distance between the two impact events, respectively. α and

Fig. 11 Impact model of particles.

v_0 denote the impact angle and impact velocity, respectively.

The entire impact process can be categorized into the following four stages:

1) The first particle impacts the surface of the target material.

2) The compression and deformation of the material surface result in Crater 1. Meanwhile, the first particle departs from the material surface.

3) The second particle impacts the surface of the target material.

4) The compression and deformation of the material surface result in Crater 2, and the second particle departs from the material surface.

When the particles successively impacted the material surface, the compression and deformation of the material surface reached a maximum when the relative impact velocity between the particles and target material was 0. When the particles collided with the target, the target material deformed elastically. Moreover, an impulse was applied such that the particles departed from the target material. It is noteworthy that when the surface of the target material deformed plastically, a crater was formed.

A study [39] was conducted to determine a time interval that allowed the stress waves in the material to be negligible after each impact. In that study, a time interval of 200 μs was selected, which is consistent with the current assumption that the second impact is due when the first impact is fully completed.

4 Numerical simulation analysis

4.1 Effect of impact distance between two impact events

In the study pertaining to the horizontal distance between the two impact events, the particle diameter, particle impact velocity, and incident angle were 5 mm, 20 m/s, and 45°, respectively. Figure 12 shows the effect of different incident positions on the crater depth. The horizontal distances of the incident positions were 0D, 0.06D, 0.1D, 0.14D, 0.2D, 0.4D, 0.6D. It is noteworthy that the second impact location was on the left side of the first impact. In Fig. 12, O and O' represent the centers of the first and second particles,
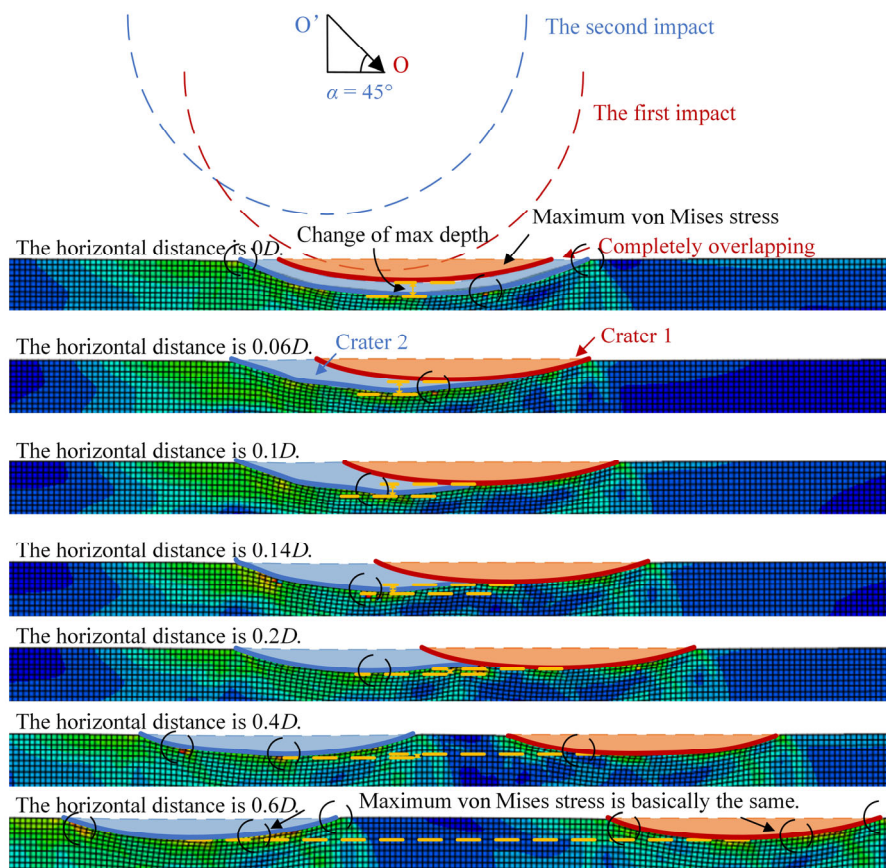

Fig. 12 Stress distribution at different distances for the particle size of 5 mm, impact velocity of 20 m/s, and impact angle of 45°.

respectively. The dotted yellow line demarcates the edges of the two craters. As shown in Fig. 12, the horizontal distance between the two impact events on the target material can be classified into four ranges. Figure 13 shows that for Range A ($u \leq 0.1D$), Crater 2 created by the second impact almost completely covered Crater 1. It was observed that the impact point of Particle 2 was located in Crater 1 generated by the first impact, whereas the maximum von Mises stress was located in Crater 2. In this case, the second impact imposed a greater effect on the target material. For Range B ($0.1D < u < 0.2D$), the impact point was located outside Crater 1. The two craters affected large areas, and the area of Crater 2 was larger than that of Crater 1. As the horizontal distance between the two impact events increased, the length of Crater 2 caused by the second impact decreased gradually. In Range C ($u = 0.2D$), the two craters resulted in overlapping areas. However, the lengths of the two crater edges were the same. In Range D ($0.2D < u < 0.6D$), the overlapping area of the two craters disappeared gradually, whereas the

affected area remained. As the horizontal distance between the two impact events increased, the von Mises stress distribution of the two craters remained constant. Moreover, the effect of the impact on the area between the two craters was negligible.

Figure 14 shows the depth difference between two craters during the impacts of a particle couplet ($H_1 - H_2$, where H_1 is the penetration depth of the first single particle, and H_2 is the penetration depth of the second particle that can impact the neighboring areas). As the horizontal distance between the two impact events changed from $0.06D$ to $0.6D$, the depth difference between the two impact events varied significantly with respect to the impact distance. When the horizontal distance between the two impact events was $0.06D$ (the second impact of the particle was located in Crater 1), the maximum depth difference was 57.5 μm, i.e., H_2 was 57.5 μm less than H_1, which indicates a significant decrease in material damage caused by the second impact on the eroded material. Additionally, as the horizontal distance between the two impact events increased from $0.1D$
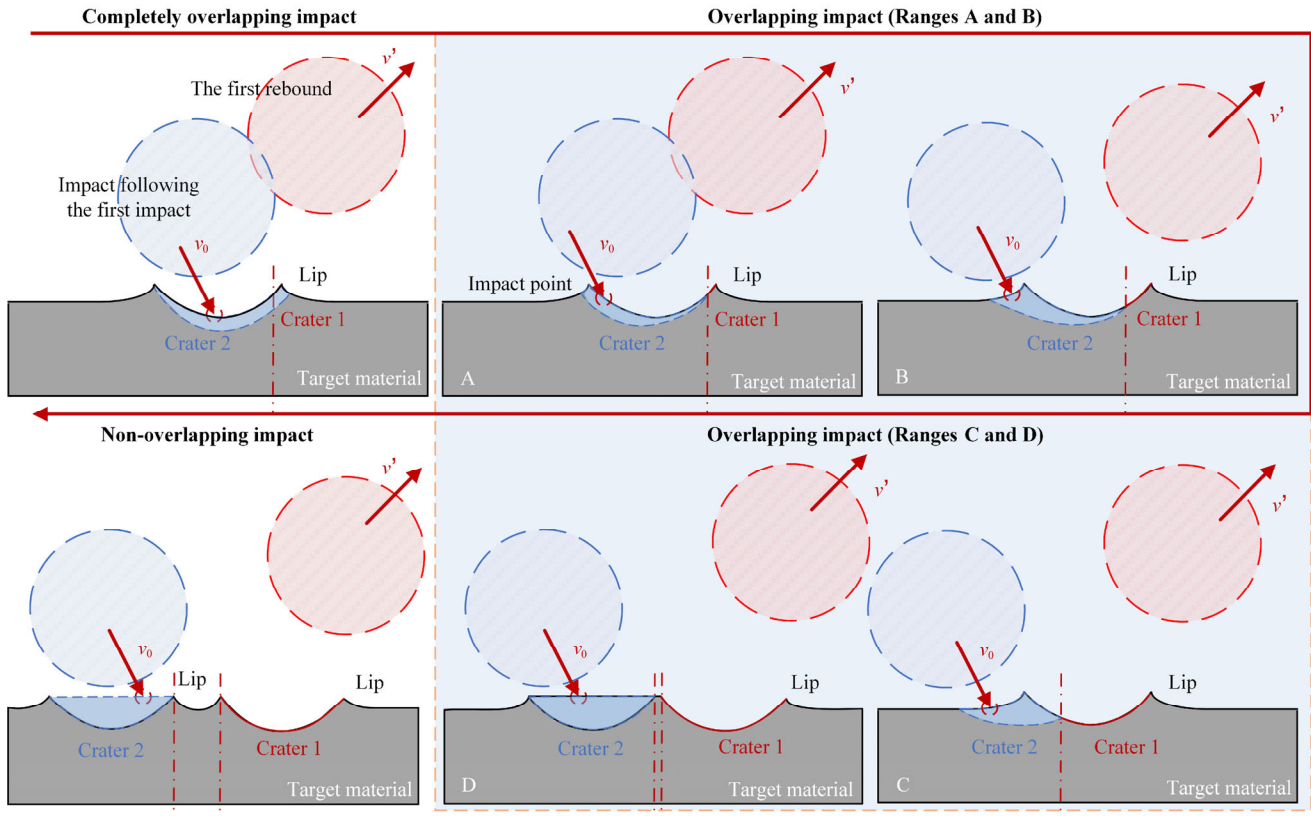

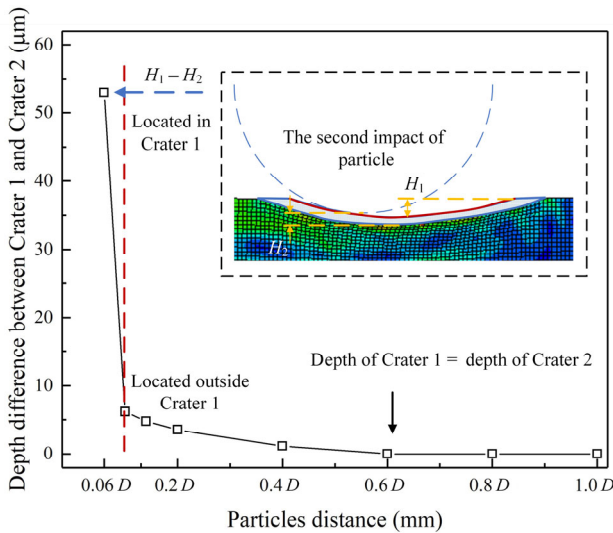**Fig. 13** Location of second impact relative to Crater 1.

Fig. 14 Depth difference between two craters against particle distance for the particle size of 5 mm, impact velocity of 20 m/s, and impact angle of 45°.

to 0.6*D* (the second impact of the particle was located outside Crater 1), the depth difference between the two craters decreased from 6.15 to 0.11 μm, i.e., crater–crater interactions diminished. At a distance of 0.6*D*, the depth of the second crater became the same as that of the first crater, which implied a complete transition from overlapping to non-overlapping impact effects.

As indicated by the residual stress distribution of the target material, the length of the affected area after the second impact was 0.6 times the particle diameter *D*. In other words, when the horizontal distance between two collisions exceeded 0.6*D*, the interaction between the two collisions was negligible. Figure 15 illustrates the affected area in this case.
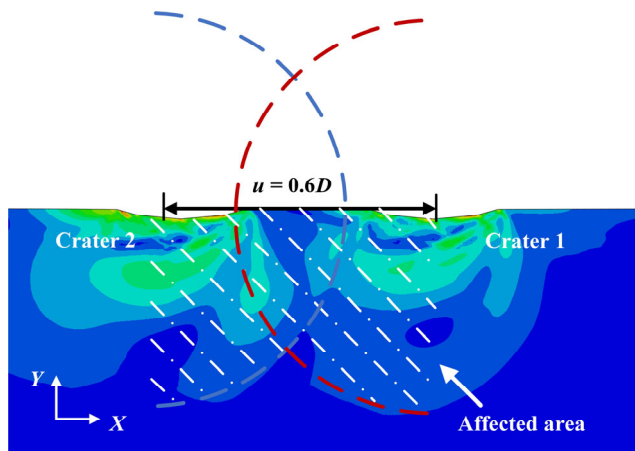
Fig. 15 Affected area by two impacting particles.

In this section, energy analysis is presented to elucidate the impact process. The energy transformation is vital for describing the particle impact process. The energy balance [31, 61] for the entire model can be mathematically expressed as

$$E_U + E_K + E_{FD} + E_W - E_{QB} = \text{Constant} \tag{8}$$

$$E_U = E_I + E_V \tag{9}$$

$$E_I = E_S + E_P + E_C \tag{10}$$

where E_U is the dissipated portion of the internal energy; E_K is the kinetic energy; E_{FD} is the energy dissipated by friction (dissipative energy refers to the energy lost during energy transfer); E_W is the work performed by external forces on the body; E_{QB} is the energy dissipated by the damping effect of solid medium infinite elements, i.e., $E_{QB} = 0$; E_I is the remaining energy, which is known as the internal energy; E_V is the energy dissipated by viscous effects, i.e., $E_V = 0$; E_S is the applied elastic strain energy; E_P is the energy dissipated by plasticity; E_C is the energy dissipated by time-dependent deformation (creep, swelling, and viscoelasticity), i.e., $E_C = 0$.

If damage occurs in the material, not all the applied elastic strain is recoverable. At any given time, the stress σ_c can be expressed in terms of the "undamaged" stress σ_u and the continuum damage parameter d as Eq. (11):

$$\sigma_c = (1 - d)\sigma_u \tag{11}$$

The damage parameter d is initiated from the value of 0 in the undamaged material, and increases to a maximum value of 1 in the fully damaged material. It is assumed that during unloading, the damage parameter remains fixed at the value achieved at time t. Therefore, Eq. (12) is obtained:

$$E_S = \int_0^t \left(\int_V (1 - d) \frac{\sigma_u}{\varepsilon_{el}} dV \right) d\tau \tag{12}$$

where ε_{el} denotes the elastic stress, V is the volume of the sample.

Moreover, the energy dissipated through the damage (E_{DWD}) is expressed as Eq. (13):

$$E_{DWD} = \int_0^t \left(\int_V (d_t - d) \frac{\sigma_u}{\varepsilon_{el}} dV \right) d\tau = \int_0^t \left(\int_V \frac{(d_t - d)}{1 - d} \frac{\sigma_c}{\varepsilon_{el}} dV \right) d\tau \tag{13}$$

where d_t denotes the damage parameters at time t.

Therefore, the energy conversion equation for this case is as Eqs. (14) and (15):

$$E_{total} = |E_{DWD}| + |E_P| + |E_K| + |E_{FD}| \tag{14}$$

$$E_I = |E_{DWD}| + |E_P| \tag{15}$$

where E_{total} is the total energy.

Equation (14) shows that the final energy loss is caused by the joint action of friction dissipation energy and damage dissipation energy. Figure 16 and Table 7 illustrate the energy change. During the entire impact
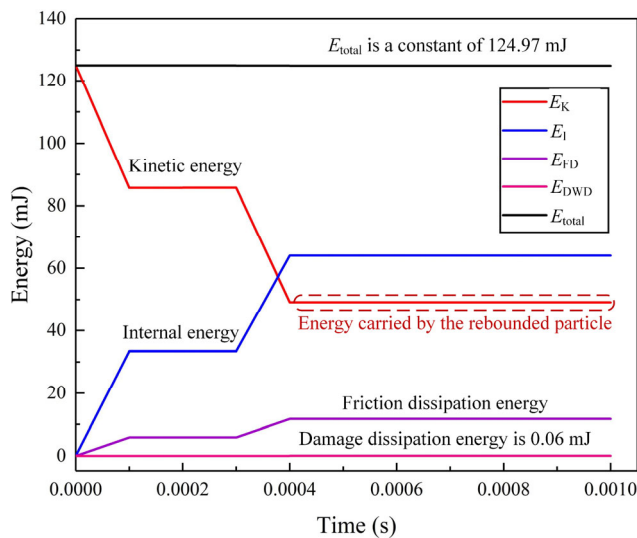
Fig. 16 Energy vs. time curve.

process, the initial kinetic energy was 124.97 mJ. The target material was subjected to the first impact of the particles at 0–0.1 ms, which resulted in plastic deformation and damage. Moreover, the second impact of the particles occurred at 0.3–0.4 ms, which further intensified the deformation and damage of the material. After the particles impacted the target, more than 80% of the energy was converted into internal energy, including a slight damage dissipation energy, and the energy dissipated by the damage was 0.06 mJ (see Fig. 16), which accounted for only 0.07% of the energy conversion. The remaining energy dissipated in the form of friction. Therefore, the change in the target morphology is mainly caused by plastic deformation, and the effect of material damage on the target morphology is negligible.

Figure 17 shows that as the horizontal distance between the two impact events increases, the internal energy of the target material initially decreased and then increased. Equation (16) and Fig. 18 show that during the impact process, owing to the energy dissipation and kinetic energy conversion, the energy conversion rate remained in the range of 48.91%–53.35%. Moreover, the kinetic energy of the particles was primarily stored in the target material in the form of internal energy.

$$\eta = \frac{W_u}{W_t} \times 100\% \tag{16}$$

where η, W_u, and W_t denote the energy conversion rate, increased internal energy of the target material, and initial kinetic energy of the particles, respectively.

Table 7 Parameters related to energy conversion based on the particle size of 5 mm, impact velocity of 20 m/s, and impact angle of 45°.

Distance between two impacts	Initial kinetic energy (mJ)	Loss of kinetic energy (mJ)	Internal energy of target (mJ)	Friction dissipating energy (mJ)	Damage dissipating energy (mJ)
0D	124.97	77.91	65.55	12.26	0.030
0.06D	124.97	74.38	61.69	12.64	0.029
0.1D	124.97	73.37	61.12	12.18	0.028
0.14D	124.97	74.35	62.35	11.93	0.029
0.2D	124.97	75.85	64.01	11.74	0.052
0.4D	124.97	78.51	66.63	11.76	0.031
0.6D	124.97	78.52	66.65	11.76	0.030
0.8D	124.97	78.51	66.63	11.77	0.030
D	124.97	78.52	66.66	78.53	0.030

Figure 18 shows that when the horizontal distance between the two impact events was approximately $0.1D$, the energy loss was the highest. Subsequently, the energy loss decreased as the horizontal distance increased. This is mainly caused by the change in the contact area between the particles and target. According to the formula $P = F/A_0$ (P is the pressure on the surface of the material; F is the applied force, where the impact velocity of the particle is constant, i.e., F is a constant value; A_0 is the contact area between the particle and material), as the contact area decreases, the resistance of the material to the particle increases gradually. This results in an increased energy loss in the material. Figure 19 presents the contact area between the particles and target.

When the horizontal distance of the second impact was within $0.06D$ (Range A), the contact area was large, and the energy loss was small. As the horizontal distance increased, the second impact occurred near the lip of Crater 1 (between A and B). Meanwhile, more kinetic energy dissipated from the material surface containing the two particles. It is noteworthy that the friction dissipation energy and damage dissipation energy remained at 11.74–12.64 mJ and 0.030–0.052 mJ, which are negligible. As the horizontal distance between the two impact events increased, the final impact of the particles occurred in the range between C and D, and the change in energy
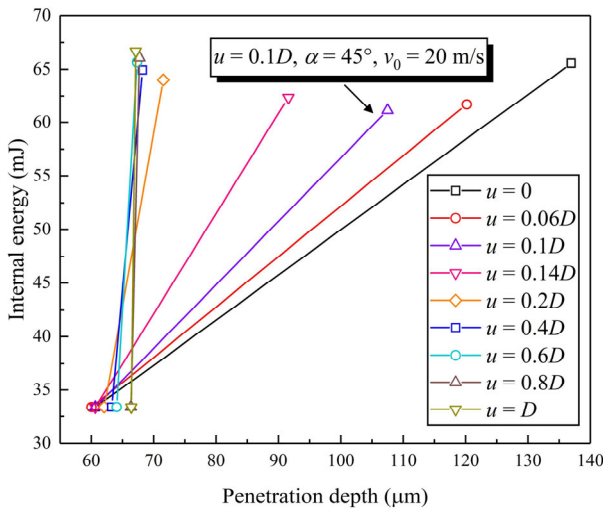
Fig. 17 Internal energy increment and depth change of target material based on the particle size of 5 mm, impact velocity of 20 m/s, and impact angle of 45°.
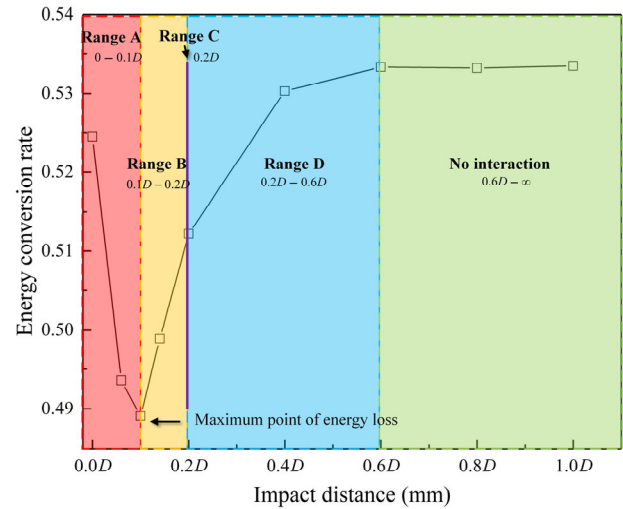

Fig. 18 Energy conversion rate for different distances between two impact events based on the particle size of 5 mm, impact velocity of 20 m/s, and impact angle of 45°.
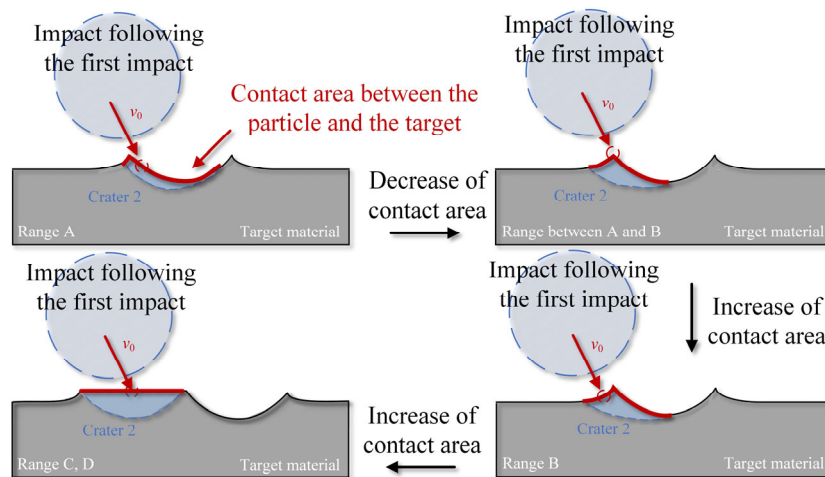

Fig. 19 Change in contact area between particles and target.

conversion reduced. When the horizontal distance exceeded 0.6*D*, the impact was similar to that of a single particle impacting the target.

4.2 Effect of impact velocity

To investigate the effect of impact velocity, the particle diameter, horizontal distance between the two impact events, and impact angle were set to 5 mm, 0.2*D*, and 45°, respectively. Moreover, the impact velocities of the two impact events were the same and were set to 14, 16, 18, 20, and 22 m/s. Figure 20 shows that as the speed increased, the depth of the crater and the difference between the depths of the two craters increased. This is because the increase in the particle velocity increased the particle forces in the normal direction, which subsequently increased the crater depth. During the second impact, as the deformation of Crater 2 increased, the material at the bottom of Crater 1 was continuously squeezed, causing it to move upward and hence resulting in a decrease in the depth of Crater 1.

The higher stress region indicates a larger deformation of the target, which resulted in a more significant erosion. Figures 20 and 21 show that as the velocity increased, the maximum stress remained in Crater 2. Moreover, as the impact velocity increased from 14 to 22 m/s, the maximum depths of the two craters increased from 38.2 to 94.5 μm. Furthermore,
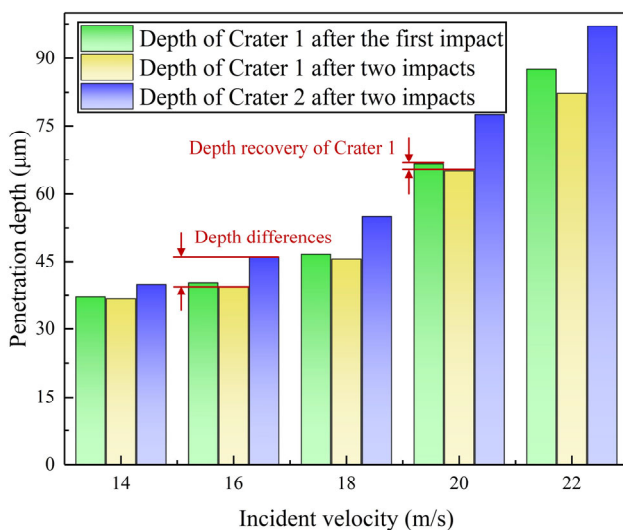

Fig. 20 Depths of two craters vs. particle velocity based on the particle size of 5 mm, impact angle of 45°, and horizontal distance of 0.2*D*.

the sizes of the two craters increased proportionally, and the contours of the craters remained unchanged. It is noteworthy that the change in the impact velocity did not significantly affect the deformation mechanism of erosion.

Figure 22 shows that as the velocity increased, the damage dissipation energy and damage to the target material increased. However, apart from the impact energy introduced to the target material that was converted into internal energy, only an insignificant portion of the impact energy dissipated in the form of damage dissipation energy. This is because the particle was spherical, and the initial velocity was low. Moreover, the damage caused by the particle impact to the target material was limited. The material mainly underwent plastic deformation instead of material removal. Therefore, impact damage to the target material accumulated gradually and can create a macro erosion morphology, e.g., in an actual oil and gas pipeline. It is noteworthy that three factors affect material damage caused by erosion as follows: number of particles, impact type (e.g., continuous), and duration.

4.3 Effect of impact angle

To investigate the effect of impact angle, the particle diameter, horizontal distance between the two impact events, and impact velocity were set to 5 mm, 0.2*D*, and 20 m/s, respectively. It is noteworthy that the characteristics of the overlapped impact were conspicuous and can be distinguished from completely overlapped and non-overlapped impact events. Moreover, the impact angles of the two impact events were set to 25°, 35°, 45°, 55°, 65°, 75°, and 85°. Figures 23 and 24 show that as the impact angle increased, the depth of the first and subsequent impact increased. When the impact angle exceeded 75°, the change in the impact depth was slight. This is because as the impact angle increased, the speed along the vertical direction increased, and the impact intensity on the target material increased as well. Because the inertial force changes the direction of the particles instead of their magnitude, the inertial force along the vertical direction $F_v = F \times \sin\alpha$, is correlated to the sine value.

As the impact angle increased from 25° to 85°, the depth difference between the two craters increased from 0.11 to 14.40 μm. Moreover, the depth difference
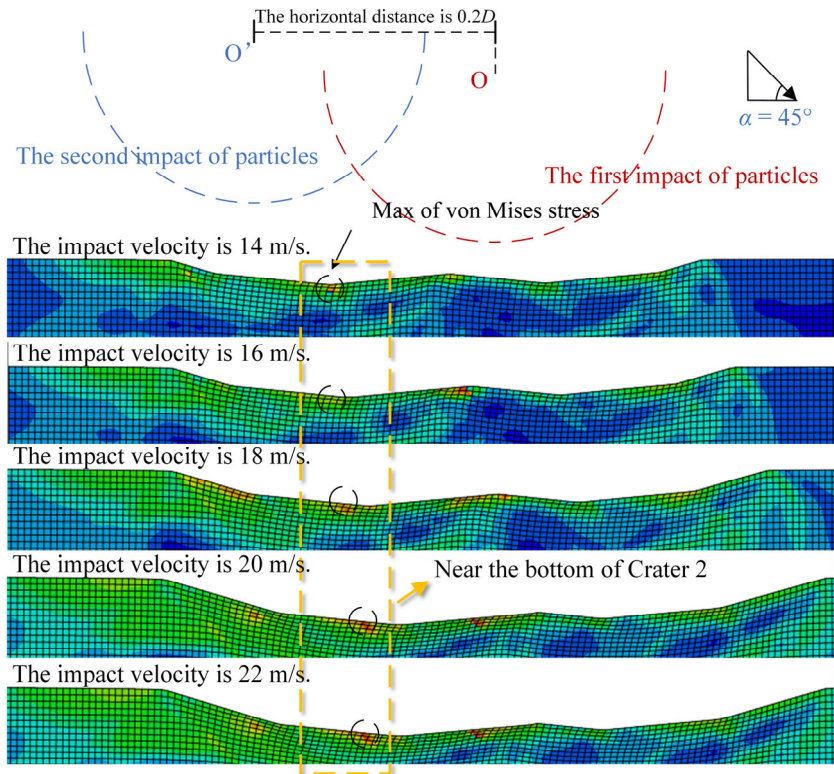
Fig. 21 Distribution of von Mises stress near crater vs. particle velocity based on the particle size of 5 mm, impact angle of 45°, and horizontal distance of 0.2*D*.
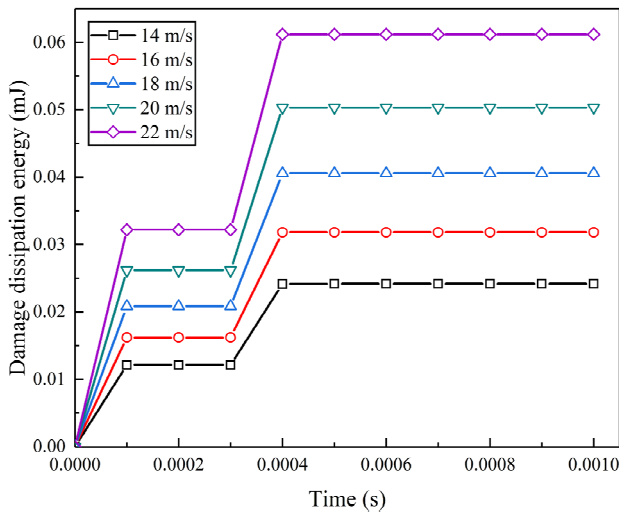

Fig. 22 Damage dissipation energy vs. time based on the particle size of 5 mm, impact angle of 45°, and horizontal distance of 0.2*D*.
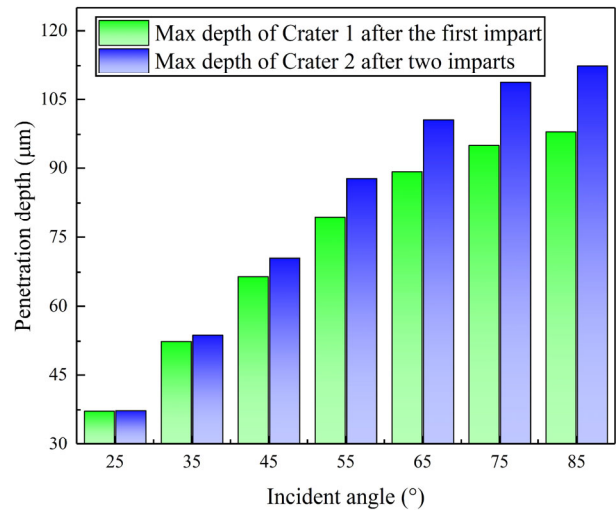
Fig. 23 Depths of two craters vs. particle angle based on the particle size of 5 mm, impact velocity of 20 m/s, and horizontal distance of 0.2*D*.

increased significantly from 45° to 55°. When the angle exceeded 55° and was affected by work hardening, the depth difference increased gradually.

Figures 25 and 26 show that when the impact angle $\alpha \leq 45°$, three stress concentration areas appeared at

the bottom and both lips of Crater 2. Moreover, when $45° \leq \alpha \leq 85°$, the two stress concentration regions were located near the bottom and left lip of the crater. No stress concentration area was observed on the lip between the two craters. This is because the large
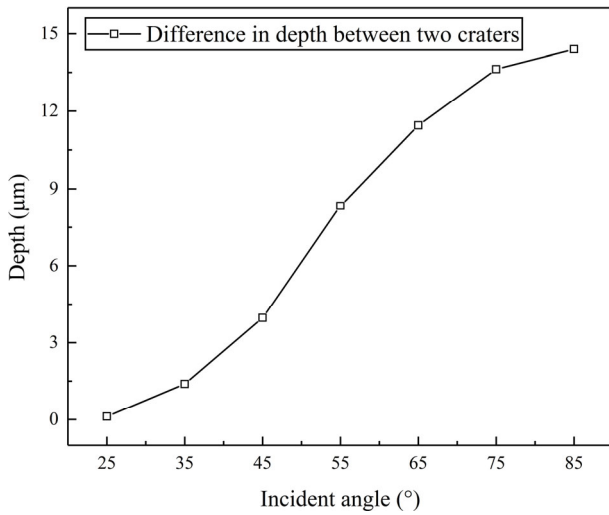
Fig. 24 Difference in depth between two craters vs. incident angle based on the particle size of 5 mm, impact velocity of 20 m/s, and horizontal distance of 0.2*D*.

plastic deformation of the target resulted in more plastic deformation after the formation of Crater 1. Therefore, surface work hardening prevented the further deformation of the target material.

Figure 27 shows that as the impact angle increased, the damage dissipation energy increased. When the

angle increased from 75° to 85°, compared with the impact angle increment from 25° to 35°, the change in energy dissipation reduced from 0.01 to 0.003 mJ. When the impact angle exceeded 75°, the change in the angle did not significantly affect the crater depth. Meanwhile, the crater morphology on the surface of the target material stabilized.

5　Modified Bitter model

To reveal the effects of adjacent craters, the internal energy variation of the target material was redefined in the modified model.

5.1　Modified model

The Bitter model is expressed mathematically as shown in Eqs. (17) and (18).

$$Q_P = \frac{1}{2} m_P \left(v_P \sin\alpha - K_B \right)^2 \tag{17}$$

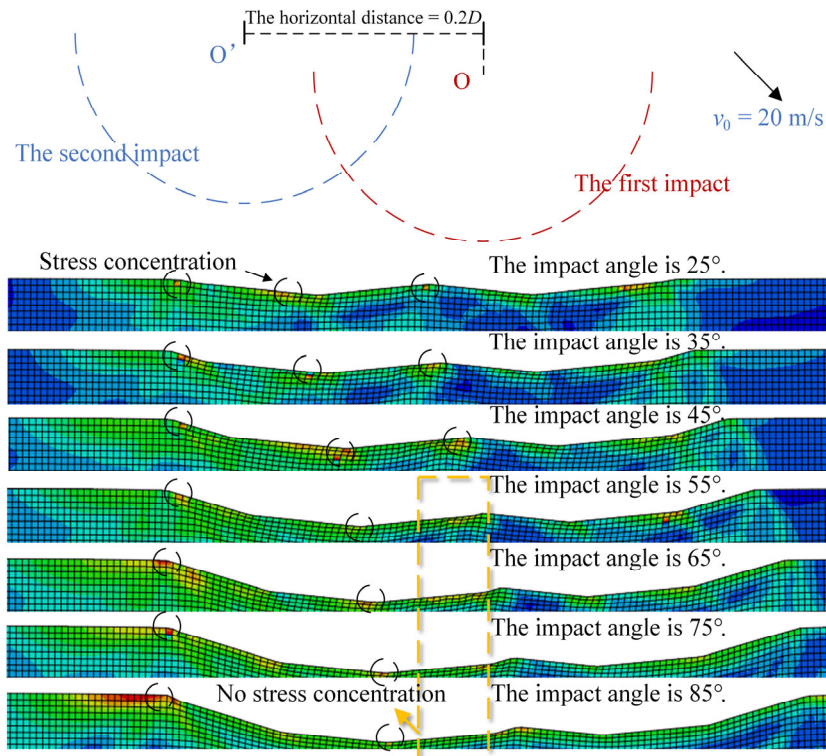$$W_D = \frac{Q_P}{\varepsilon_B} \tag{18}$$

Fig. 25 Distribution of von Mises stress near crater vs. particle angle (°) based on the particle size of 5 mm, impact velocity of 20 m/s, and horizontal distance of 0.2*D*.
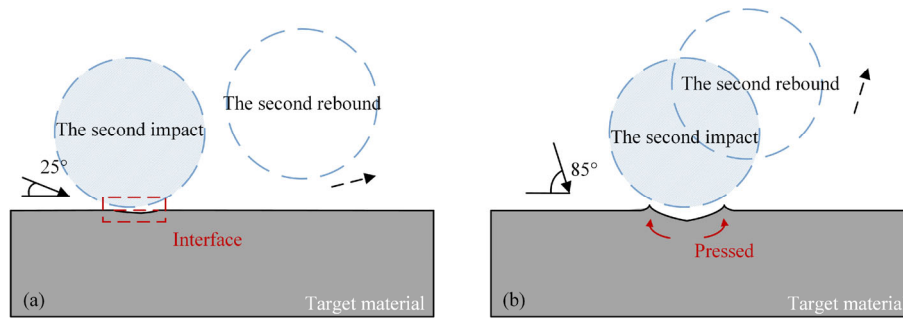
Fig. 26 Effect of angle on the second impact: (a) type of surface damage caused by particles at low angles; (b) type of surface damage caused by particles at high angles.
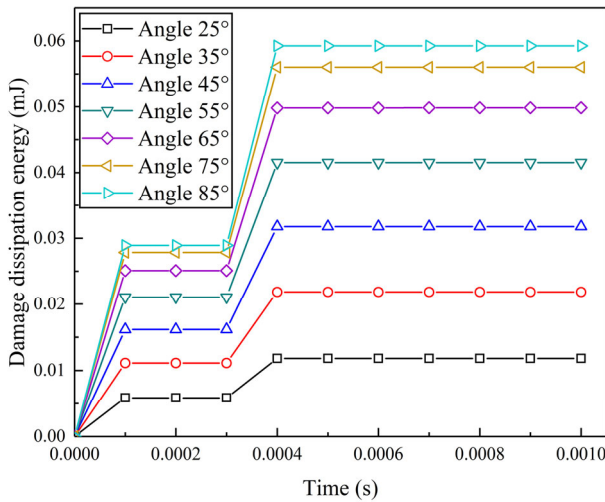

Fig. 27 Damage dissipation energy vs. time based on the particle size of 5 mm, impact velocity of 20 m/s, and horizontal distance of 0.2D.

where Q_p is the formation of the permanent indentation, which requires a certain amount of energy; m_p is the quality of the abrasive particle; α is the impact angle of the particle; K_B is a constant related to the velocity of the particle before collision; W_D is the wear due to repeated deformation; and ε_B is the deformation wear factor.

The effects of the impact velocity, impact angle, and horizontal distance between two craters on the internal energy were revised using the First Optimization (1stOpt) fitting software. Hence, the modified energy (Q_{pz}) was replaced by the Bitter model. The modified model is expressed as Eq. (19):

$$Q_{pz} = \left(2.2 \times 10^{-4} D - 0.02 D^{0.48} + 1.56 \times 10^{-3}\right)$$
$$\left(1.94 \times 10^{-4} v_p^{5.85} - 4789.32 v_p + 2447.54 v_p^{1.66}\right)$$
$$\left(0.24 \sin \alpha - 0.15 \cos \alpha + 0.098\right) \tag{19}$$

5.2 Model verification

As shown in Fig. 28, the calculation results of the fitting formula are similar to the calculation data of the model. In addition, four evaluation indicators, i.e., RMSE (root mean square error), SSE (sum of squares due to error), R (correlation coefficient), and R^2 (square of correlation coefficient), were used to assess the quality of the fitting results. The values of RMSE and SSE were approximately 0, whereas the values of R and R^2 were approximately 1. Hence, this formula can characterize the simulation results accurately.
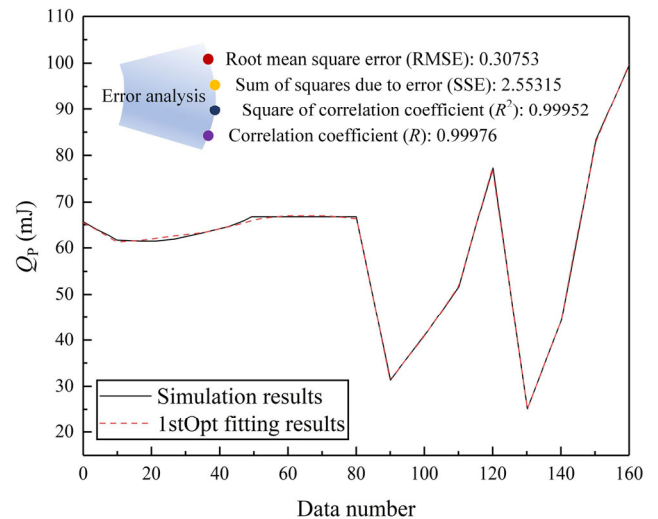

Fig. 28 Relationship between calculated results and simulated data.

6 Conclusions

In the present study, considering the JC hardening criterion and JC damage criteria, a numerical model for simulating overlapping collisions of spherical

particles on AA6061 aluminum alloy was established. Moreover, the accuracy of the model was verified by comparing the results obtained with the experimental results. The following conclusions were obtained from this study:

1) The impact location of the neighboring particles, which is defined as the horizontal distance between the solid particle impacting location, significantly affects the erosion magnitude and pattern. As the horizontal distance between the two impact events increased from 0 to 0.6 times the particle diameter, the interaction between the formed craters reduced gradually. When the horizontal distance exceeded 0.6 times the particle diameter, the interaction between two craters disappeared.

2) As the horizontal distance between the two impact events changed from $0.06D$ to $0.6D$, the depth difference between the two impact events changed significantly with respect to the impact distance. When the horizontal distance between the two impacts was $0.06D$, the maximum depth difference was 57.5 µm. The impact on existing craters can significantly decelerate erosion. As the horizontal distance between the two impact events increased from $0.1D$ to $0.6D$, the depth difference between two craters decreased from 6.15 to 0.11 µm, which implies diminished crater–crater interactions.

3) As the horizontal distance between impact events increased, the energy conversion rate during the impact initially decreased rapidly. Subsequently, it increased gradually after it reached a critical point, which was 0.1 times the particle diameter.

4) As the impact velocity increased from 14 to 22 m/s, the depth of the crater increased from 38.2 to 94.5 µm, whereas the profile of the two craters remained unchanged.

5) The removal of the target material by the impact particles was limited by plastic deformation erosion. Moreover, the change in the target morphology was mainly caused by plastic deformation. The continuous impact and long-term accumulation of numerous particles contributed significantly to pipeline erosion.

6) The second impact was hindered by work hardening as the depth increased. This resulted in an area without stress concentration on the lip between the craters, which decelerated the erosion of the material.

References

[1] Zheng C, Liu Y H, Wang H X, Zhu H Y, Liu Z K, Cai B P, Shen Y. Numerical study on improving the erosion life of ball seat for oil and gas reservoir fracturing. *Eng Fail Anal* **60**: 188–198 (2016)

[2] Grewal H S, Agrawal A, Singh H. Slurry erosion performance of Ni–Al$_2$O$_3$ based composite coatings. *Tribol Int* **66**: 296–306 (2013)

[3] Ahmed D H, Naser J, Deam R T. Particles impact characteristics on cutting surface during the abrasive water jet machining: Numerical study. *J Mater Process Technol* **232**: 116–130 (2016)

[4] Ojala N, Valtonen K, Antikainen A, Kemppainen A, Minkkinen J, Oja O, Kuokkala V T. Wear performance of quenched wear resistant steels in abrasive slurry erosion. *Wear* **354–355**: 21–31 (2016)

[5] Tarodiya R, Gandhi B K. Hydraulic performance and erosive wear of centrifugal slurry pumps—A review. *Powder Technol* **305**: 27–38 (2017)

[6] Darihaki F, Hajidavalloo E, Ghasemzadeh A, Safian G A. Erosion prediction for slurry flow in choke geometry. *Wear* **372–373**: 42–53 (2017)

[7] Parsi M, Najmi K, Najafifard F, Hassani S, McLaury B S, Shirazi S A. A comprehensive review of solid particle erosion modeling for oil and gas wells and pipelines applications. *J Nat Gas Sci Eng* **21**: 850–873 (2014)

[8] Levy A V. The platelet mechanism of erosion of ductile metals. *Wear* **108**(1): 1–21 (1986)

[9] Levy A V. The erosion of structural alloys, cermets and *in situ* oxide scales on steels. *Wear* **127**(1): 31–52 (1988)

[10] Sheldon G L, Kanhere A. An investigation of impingement erosion using single particles. *Wear* **21**(1): 195–209 (1972)

[11] Marshall D B, Evans A G, Gulden M E, Routbort J L, Scattergood R O. Particle size distribution effects on the solid particle erosion of brittle materials. *Wear* **71**(3): 363–373 (1981)

[12] Finnie I. Erosion of surfaces by solid particles. *Wear* **3**(2): 87–103 (1960)

[13] Bitter J G A. A study of erosion phenomena part I. *Wear* **6**(1): 5–21 (1963)

[14] Bitter J G A. A study of erosion phenomena: Part II. *Wear* **6**(3): 169–190 (1963)

[15] Hutchings I M, Winter R E, Field J E. Solid particle erosion of metals: The removal of surface material by spherical projectiles. *P Roy Soc A-math Phy* **348**(1654): 379–392 (1976)

[16] Hutchings I M. Deformation of metal surfaces by the oblique impact of square plates. *Int J Mech Sci* **19**(1): 45–52 (1977)

[17] Hutchings I M, Macmillan N H, Rickerby D G. Further studies of the oblique impact of a hard sphere against a ductile solid. *Int J Mech Sci* **23**(11): 639–646 (1981)

[18] Quadir T, Shewmon P. Solid particle erosion mechanisms in copper and two copper alloys. *Metall Trans A* **12**(7): 1163–1176 (1981)

[19] Hutchings I M, Winter R E. Particle erosion of ductile metals: A mechanism of material removal. *Wear* **27**(1): 121–128 (1974)

[20] Sahoo R, Jha B B, Sahoo T K, Mantry S. Effect of microstructural degradation on solid particle erosion behavior of 2.25Cr-1Mo steel. *Tribol Trans* **57**(4): 679–689 (2014)

[21] Tirupataiah Y, Venkataraman B, Sundararajan G. The nature of the elastic rebound of a hard ball impacting on ductile, metallic target materials. *Mater Sci Eng A* **124**(2): 133–140 (1990)

[22] Papini M, Dhar S. Experimental verification of a model of erosion due to the impact of rigid single angular particles on fully plastic targets. *Int J Mech Sci* **48**(5): 469–482 (2006)

[23] Dhar S, Krajac T, Ciampini D, Papini M. Erosion mechanisms due to impact of single angular particles. *Wear* **258**(1–4): 567–579 (2005)

[24] Shimizu K, Noguchi T, Seitoh H, Okada M, Matsubara Y. FEM analysis of erosive wear. *Wear* **250**(1–12): 779–784 (2001)

[25] Shimizu K, Noguchi T, Seitoh H, Muranaka E. FEM analysis of the dependency on impact angle during erosive wear. *Wear* **233–235**: 157–159 (1999)

[26] ElTobgy M S, Ng E, Elbestawi M A. Finite element modeling of erosive wear. *Int J Mach Tools Manuf* **45**(11): 1337–1346 (2005)

[27] Junkar M, Jurisevic B, Fajdiga M, Grah M. Finite element analysis of single-particle impact in abrasive water jet machining. *Int J Impact Eng* **32**(7): 1095–1112 (2006)

[28] Li W Y, Wang J, Zhu H T, Li H Z, Huang C Z. On ultrahigh velocity micro-particle impact on steels—A single impact study. *Wear* **305**(1–2): 216–227 (2013)

[29] Guo Y B, Yen D W. A FEM study on mechanisms of discontinuous chip formation in hard machining. *J Mater Process Technol* **155–156**: 1350–1356 (2004)

[30] Forder A, Thew M, Harrison D. A numerical investigation of solid particle erosion experienced within oilfield control valves. *Wear* **216**(2): 184–193 (1998)

[31] Ben-Ami Y, Levy A. Absorbed shear energy during solid particle impact on ductile surface. *Wear* **368–369**: 162–172 (2016)

[32] Pan J J, Hu S S, Niu A N, Ding K Y, Yang L J. Numerical analysis of particle impacting and bonding processes during high velocity oxygen fuel spraying process. *Appl Surf Sci* **366**: 187–192 (2016)

[33] Li W Y, Liao H L, Li C J, Bang H S, Coddet C. Numerical simulation of deformation behavior of Al particles impacting on Al substrate and effect of surface oxide films on interfacial bonding in cold spraying. *Appl Surf Sci* **253**(11): 5084–5091 (2007)

[34] Takaffoli M, Papini M. Finite element analysis of single impacts of angular particles on ductile targets. *Wear* **267**(1–4): 144–151 (2009)

[35] Monaghan J J. An introduction to SPH. *Comput Phys Commun* **48**(1): 89–96 (1988)

[36] Shao J R, Li H Q, Liu G R, Liu M B. An improved SPH method for modeling liquid sloshing dynamics. *Comput Struct* **100–101**: 18–26 (2012)

[37] Johnson G R, Stryk R A, Beissel S R. SPH for high velocity impact computations. *Comput Methods Appl Mech Eng* **139**(1–4): 347–373 (1996)

[38] Aktay L, Johnson A F. FEM/SPH coupling technique for high velocity impact simulations. In: *Advances in Meshfree Techniques*. Dordrecht (the Netherlands): Springer Netherlands, 1970: 147–167.

[39] Deliwala A A, Peter M R, Yerramalli C S. A multiple particle impact model for prediction of erosion in carbon-fiber reinforced composites. *Wear* **406–407**: 185–193 (2018)

[40] Cao X W, Fu C Y, Xie Z Q, Wu C, Sun X Y. Simulation and experimental study on the surface morphology and energy lost of the target material under non-overlapping impact of angular particles. *Chin J Chem Eng* **29**: 47–56 (2021)

[41] Zang X R, Cao X W, Zhang J, Xie Z Q, Xiong N, Darihaki F, Bian J. Investigation of surface damage of ductile materials caused by rotating particles. *Wear* **488–489**: 204185 (2022)

[42] Vyas D R, Cummins S J, Rudman M, Cleary P W, Delaney G W, Khakhar D V. Collisional SPH: A method to model frictional collisions with SPH. *Appl Math Model* **94**: 13–35 (2021)

[43] Hausberger A, Major Z, Theiler G, Gradt T. Observation of the adhesive- and deformation- contribution to the friction and wear behaviour of thermoplastic polyurethanes. *Wear* **412–413**: 14–22 (2018)

[44] Hassanamraji N, Eivani A R, Aboutalebi M R. Finite element simulation of deformation and heat transfer during friction stir processing of as-cast AZ91 magnesium alloy. *J Mater Res Technol* **14**: 2998–3017 (2021)

[45] Hao G N, Dong X W, Du M C, Li Z L, Dou Z C. A comparative study of ductile and brittle materials due to single angular particle impact. *Wear* **428–429**: 258–271 (2019)

[46] Arabnejad H, Uddin H, Panda K, Talya S, Shirazia S A. Testing and modeling of particle size effect on erosion of steel and cobalt-based alloys. *Powder Technol* 394: 1186–1194 (2021)

[47] Hutchings I M. A model for the erosion of metals by spherical particles at normal incidence. *Wear* **70**(3): 269–281 (1981)

[48] Beckmann G, Gotzmann J. Analytical model of the blast wear intensity of metals based on a general arrangement for abrasive wear. *Wear* **73**(2): 325–353 (1981)

[49] Dhar S, Krajac T, Ciampini D, Papini M. Erosion mechanisms due to impact of single angular particles. *Wear* **258**(1–4): 567–579 (2005)

[50] Briscoe B J. Contact mechanics. *Tribol Int* **19**(2): 109–110 (1986)

[51] Lemaitre J. Evalution of dissipation and damage in metals submitted to dynamic loading, mechanical behavior of materials. In: Proceedings of the International Conference on Materials, Kyoto, Japan, 1972: 540–549.

[52] Johnson G R, Cook W H. Fracture characteristics of three metals subjected to various strains, strain rates, temperatures and pressures. *Eng Fract Mech* **21**(1): 31–48 (1985)

[53] Tanimura S, Tsuda T, Abe A, Hayashi H, Jones N. Comparison of rate-dependent constitutive models with experimental data. *Int J Impact Eng* **69**: 104–113 (2014)

[54] Takaffoli M, Papini M. Material deformation and removal due to single particle impacts on ductile materials using smoothed particle hydrodynamics. *Wear* **274–275**: 50–59 (2012)

[55] Hernandez C, Maranon A, Ashcroft I A, Casas-Rodriguez J P. A computational determination of the Cowper-Symonds parameters from a single Taylor test. *Appl Math Model* **37**(7): 4698–4708 (2013)

[56] Oka Y I, Okamura K, Yoshida T. Practical estimation of erosion damage caused by solid particle impact. *Wear* **259**(1–6): 95–101 (2005)

[57] Erosive Wear in Piping Systems. Report, DNV RPO501, DNV, Norway, 2007.

[58] Arabnejad H, Mansouri A, Shirazi S A, McLaury B S. Development of mechanistic erosion equation for solid particles. *Wear* **332–333**: 1044–1050 (2015)

[59] Piao M J, Huh H, Lee I, Park L. Characterization of hardening behaviors of 4130 Steel, OFHC Copper, Ti6Al4V alloy considering ultra-high strain rates and high temperatures. 131-132: 1117-1129 (2017)

[60] Hadavi V, Papini M. Numerical modeling of particle embedment during solid particle erosion of ductile materials. *Wear* **342–343**: 310–321 (2015)

[61] Zheng C, Liu Y H, Chen C, Qin J, Ji R J, Cai B P. Numerical study of impact erosion of multiple solid particle. *Appl Surf Sci* **423**: 176–184 (2017)

[62] Dong X W, Li Z L, Feng L, Sun Z C, Fan C Y. Modeling, simulation, and analysis of the impact(s) of single angular-type particles on ductile surfaces using smoothed particle hydrodynamics. *Powder Technol* **318**: 363–382 (2017)

[63] Kita A, Cavalagli N, Masciotta M G, Lourenço P B, Ubertini F. Rapid post-earthquake damage localization and quantification in masonry structures through multidimensional non-linear seismic IDA. *Eng Struct* **219**: 110841 (2020)

Xuerui ZANG. He obtained his bachelor's degree from the Petroleum Engineering College of Yangtze University in 2020. Now he works with Prof. Xuewen CAO as a student of Ph.D. in the College of Pipeline and Civil Engineering, China University of Petroleum (East China). His interested research area includes erosion wear, pipe-soil interaction, and multi-phase flow.

Xuewen CAO. He obtained his bachelor's degree of Engineering and Ph.D. degree in 1989 and 2006 from East China Petroleum Institute and Xi'an Jiaotong University, respectively. Now he is a professor and tutor of Ph.D. students in major oil and gas storage and transportation engineering. His interested research areas include multi-phase flow, erosion, offshore oil, supersonic nozzle, gas pipeline integrity management, and natural gas treatment and processing. He successively presided and participated in many research projects like "the National Science and Technology Major Project" and "the National Natural Science Foundation of China". He has published more than 150 papers in leading journals.